ACS OMEGA

http://pubs.acs.org/journal/acsodf

Article

Effect of Ionic Mass Transport on the Performance of a Novel Tubular Direct Carbon Fuel Cell for the Maximal Use of a Carbon-Filled Porous Anode

Raihan Choudhury, Ah-Hyun Kang, and Donggeun Lee*

Cite This: *ACS Omega* 2022, 7, 31003−31012

Read Online

ACCESS | Metrics & More | Article Recommendations | Supporting Information

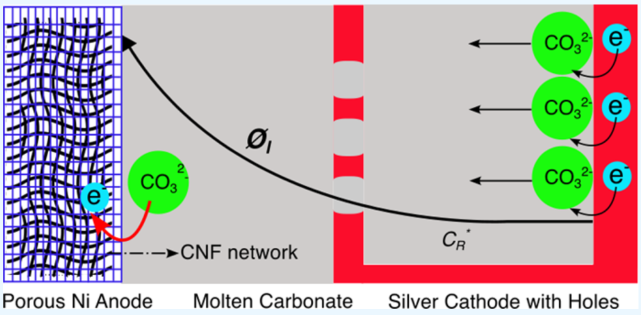

ABSTRACT: Despite a large number of existing studies about direct carbon fuel cells (DCFCs), sufficient power generation has remained a major technical challenge for the commercialization of DCFCs. This study was designed to implement the benefits of a carbon-filled porous anode developed in our recent studies in a unit cell. First, we developed a new tubular cell assembly comprising an anode, a thin matrix, and a tubular cathode with a certain number of holes in its surface. By employing a reference electrode, we measured the resistance and *I*−*V*−*P* characteristics of the anode, a cathode with a single hole, and the entire cell. As a result, we found that the cathode performance was degraded by resistance to ionic mass transfer, while the anode resistance was invariant (∼0.4 Ω cm^2). By developing a semi-empirical current−potential model including an ion mass transport effect, we proved that the number of holes in the cathode surface is the key to the maximal utilization of the present anode. This eventually led to notable gains in the maximum power density to 205 mW cm^{-2} at 700 °C in experiments. Lastly, a durability test was conducted to reconfirm the effect of ionic mass transfer on the power generation over time.

1. INTRODUCTION

Burning coal to generate electricity remains an established and economical method for the utilization of coal.[1] However, the process poses daunting challenges to the environment, such as high emission of greenhouse gases and particulate matter. A direct carbon fuel cell (DCFC) was considered as an ideal alternative (to combustion) for using coal more efficiently and with less environmental impact. In fact, DCFCs are known to operate with near 100% thermal efficiency and with an ease of CO_2 capture relative to that of coal-burning industries, which has prompted a large number of fundamental studies on DCFCs.[2−10]

Theoretically, an anode reaction takes place in molten carbonate (MC)-based DCFC systems between carbon (C) and nearby carbonate ions (CO_3^{2-}) in a pool of the MC electrolyte, resulting in the production of CO_2 and electrons,[4] as shown in eq 1.

$$C + 2CO_3^{2-} \rightarrow 3CO_2 + 4e \tag{1}$$

The carbonate ions are produced on the cathode by the electrochemical reduction reaction between oxygen (O_2) and carbon dioxide (CO_2) in accordance with eq 2. They are then transported through the MC electrolyte to the anode.[1] Because carbonate ions are available only in the MC electrolyte, the carbon must be in simultaneous contact with the electrolyte to produce electrons and with the anode to collect the electrons. The mutual contact area between the fuel, anode, and electrolyte is known as the triple phase boundary (TPB), and it determines the activity of the anode.

$$O_2 + 2CO_2 + 4e \rightarrow 2CO_3^{2-} \tag{2}$$

Likewise, eq 2 indicates that the gas mixture should be in contact with the cathode and electrolyte to create and transport the carbonate ions, respectively. One may notice that the extent of this contact can also determine the activity of the cathode. Because the overall cell reaction is the result of three consecutive reactions—anode reaction, ion diffusion, and cathode reaction in series—any of the elementary reactions, if insufficient, can limit the overall cell performance.[1]

There have been extensive efforts to increase anode and cell performance by testing a variety of materials and structures for use as anodes and fuels and by utilizing different types and compositions of the electrolyte.[10−14] For instance, Kulkarni et al.[15] employed an anode of $La_{0.6}Sr_{0.4}Co_{0.2}Fe_{0.8}O_{3\pm\delta}$ (LSCF)

Received: May 14, 2022
Accepted: August 10, 2022
Published: August 23, 2022

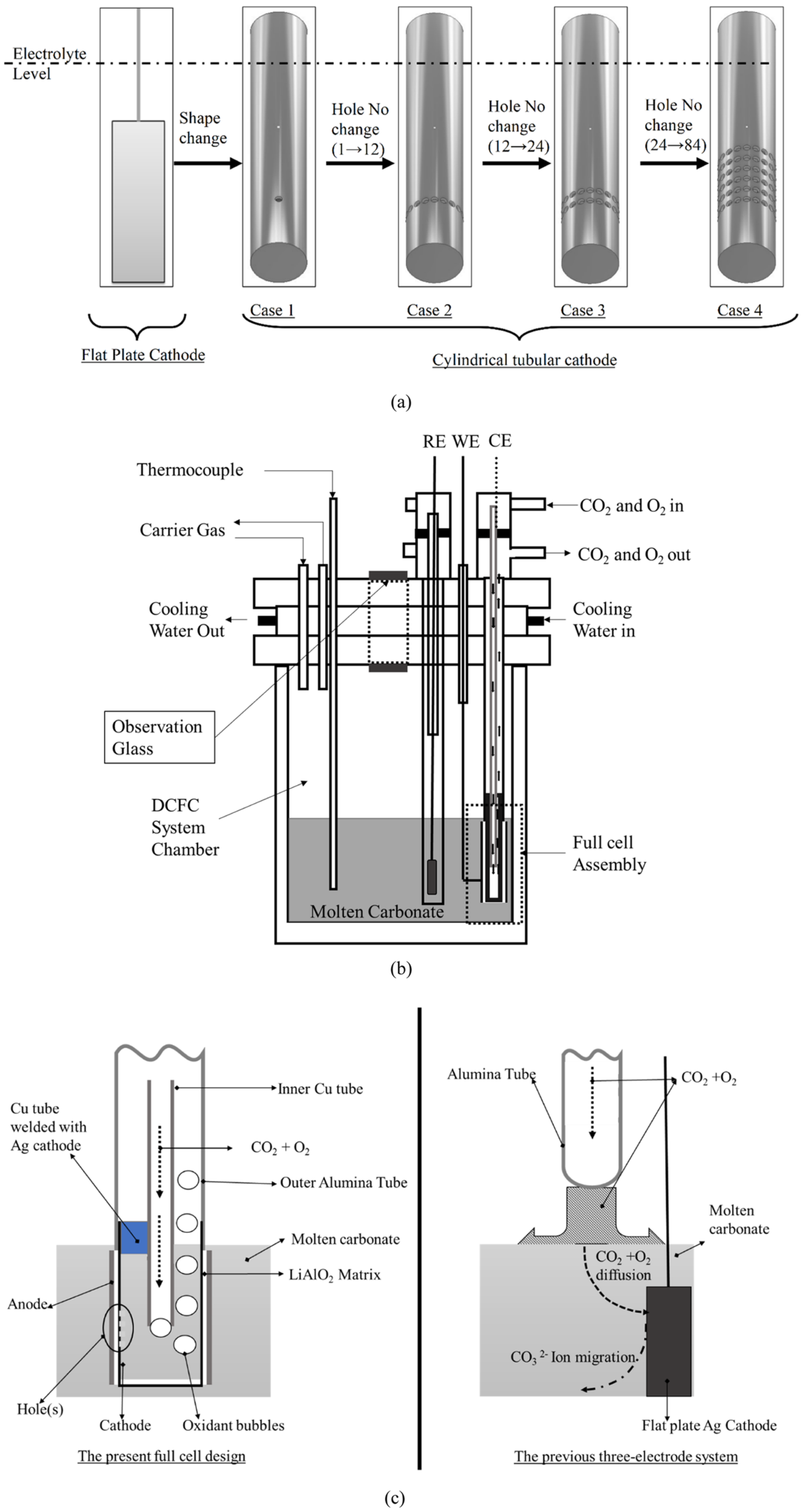

Figure 1. Features of the present tubular MC−DCFC system: (a) design change in the cathode tube, (b) experimental setup of the entire system consisting of a WE, a CE, and an RE, and (c) schematic illustration of the difference in oxidant gas supply to the cathode (CE) between the present cell and the previous system.

with carbon black and micronized graphite as fuel and reported a moderate maximum power density (MPD) of 42 mW cm^{-2} at 800 °C. Because LSCF is known to have low electronic conductivity and an unstable anode structure in reducing atmosphere at high temperatures, porous Ni/NiO-yttria-stabilized zirconia (YSZ) or Ni/NiO-scandium-stabilized zirconia (ScSZ) has often been used to circumvent the drawbacks of LSCF. Liu et al.[16] developed an anode-supported tubular DCFC in which the anode was modified with a NiO/ScSZ functional layer, resulting in an increase of the MPD to up to 104 mW cm^{-2} at 850 °C. Similarly, a Ni/samarium-doped ceria (SDC) on an SDC electrolyte was tested as a mixed ionic and electronic conductor (MIEC) anode, particularly for lowering the operation temperature, but the MPD still remained below 100 mW cm^{-2} at 650 °C.[17] Overall, those solid MIEC anodes on a solid electrolyte turn out not to be as effective as expected for extending TPB sites beyond the two-dimensional anode-electrolyte interface, even at high temperatures.

Here, it is worth noting that remarkable progress in increasing MPD has been observed in hybrid DCFC systems using MC as a redox mediator[18] or using molten metal.[19] Similar to Ju et al.,[20] who loaded a mixture of Sn and carbon fuel on a Ni-YSZ anode, Jayakumar et al.[19] developed a mixed fuel molten metal Sb anode/ScSz system and reported 350 mW cm^{-2} at 700 °C. That this notable result was obtained at an intermediate temperature was attributed to the excellent function of the molten Sb as a redox mediator ($2Sb + 3O^{2-} \rightarrow Sb_2O_3 + 6e$ and $Sb_2O_3 + 3/2C \rightarrow 2Sb + 3/2CO_2$), relative to the performance of other low-melting point metals, such as Bi, Si, and Pb. Clearly, this system requires a perfect suspension of fuel particles in the melt of Sb and Sb_2O_3 for the maximal utilization of Sb, just as with the concept of the aforementioned TPB, which limits the use of some fuels in this system (such as a sugar char, which has a density similar to that of the molten metal). Jiang et al.[18] loaded a mixture of fuel and carbonates on a Ni-YSZ anode/YSZ electrolyte and reported that the highest MPD was 878 mW cm^{-2} at 850 °C. This seems to indicate that the first hurdle for the commercialization of DCFCs has been overcome.

However, it should be recalled that the potential benefits of DCFCs are realized only when using the direct electrochemical oxidation of carbon in the solid phase, not through the conversion of carbon to gaseous fuels such as CO. It is interesting to notice that the previous promising improvements in MPD have been attained mostly at high temperatures (>700 °C), where most carbon fuels are converted to CO through the Boudouard reaction ($C + CO_2 = 2CO$).[10,18,19] This implies that MPD still remains a technical challenge in DCFCs, which turned our attention back to fundamental questions of how much MPD could increase and what the intrinsic limit would be without any contribution from gaseous fuels.

Recently, we proposed two novel ideas to increase the MPD to the limit based on TPB formation in a porous Ni anode. For example, Li et al.[21] directly generated three types of pure carbon nanoparticles in a porous Ni anode through thermal decomposition of gaseous hydrocarbons and then tested a carbon-filled porous anode with a three-electrode MC–DCFC system at 700 °C. The results were promising for increasing the anode MPD well beyond 500 mW cm^{-2} if the best control of morphology and crystallinity of carbon could be achieved. Another trial[22] was used to flow graphite powder–MC slurry through a porous Ni anode at 700 °C, which enabled a notable increase of the anode MPD to 645 mW cm^{-2} upon the best size matching between the fuel particles and anode pores in a pool of MC. The enhanced anode performance was attributed to a dramatic increase of TPB sites and the resulting decrease of anode resistance below 0.1 Ω cm^2. It should be noted that this result was attained simply by increasing the physical contact between the fuel particles and anode, even with pure carbons that contain the least amounts of gaseous species and catalytic ashes, such as in conventional coals or biomass.[23] This suggests that the intrinsic limit of anode MPD from the solid-state electrochemical oxidation of carbon is comparable to the MPD level of hydrogen-fueled fuel cells [e.g., MPD > 978 mW cm^{-2} for a proton exchange membrane fuel cell (PEMFC)[24]]. Another potential benefit of our approaches would be to enable an easy, at least intermittently continuous fuel supply, which might solve the other critical challenge with DCFCs (i.e., long-term operation).[25,26]

Noting that our previous studies[21,22] were all about fuel-filled anodes and their performance, the initial objective of this study was to verify the performance increase at the level of a full cell. We developed a new tubular cell assembly consisting of a carbon-filled porous anode, a thin matrix, and a tubular cathode with a certain number of holes for carbonate ion transport. In a series of preliminary experiments, we measured the resistance of the components and of the full cell to verify that the cathode with a single hole exhibited a high level of mass transfer resistance, in fact, the major part of cell resistance. Based on the result, we developed a semi-empirical current–potential model to figure out how many holes are most effective for reducing the cathode resistance and why. Finally, we performed a durability test for the two cells with a single hole or multiple holes to reconfirm the effect of ionic transport passage on MPD over the lifetime.

2. MATERIALS AND METHODS

The present tubular cathode-supported full cell was prepared as follows. First, a 7.2 mm-diameter, closed-bottom silver tube was employed as a cathode. Different numbers of 1.0 mm holes were drilled into the side walls of silver tubes, starting from a single hole for case 1 to 12, 24, and 84 holes for cases 2, 3, and 4 (Figure 1a), respectively, to control the total area of openings available for ion transport. For comparison, a flat-plate silver cathode used in our previous work[21−23] was also considered. Second, a 1.2 mm thick porous Ni foam with a pore size of 50–75 μm was tightly wrapped on the silver tube, the surface of which was coated with a 1.2 mm thick ceramic matrix separating the two electrodes. Third, the anode–matrix–cathode assembly was installed in a quartz tube and then placed in the middle of a hot-wall tube furnace maintained at 500 °C. Propane gas was made to flow through the annular space of Ni foam at a rate of 55 mL min^{-1}, leading to the formation of carbon nanofibers (CNF) in the pore region of the Ni foam. This thermal decomposition reaction was set to continue until the carbon loading in the Ni networks reached 5% by mass. The carbon-loaded porous Ni foam was detached from the cathode-supported anode assembly and then cut into slices for the subsequent visualization using a scanning electron microscope (Carl Zeiss AG—Supra 25, 10 kV). Figure S1 in the Supporting Information compares the scanning electron microscopy (SEM) images of the Ni foam before and after the carbon formation. Details of the carbon production method are available elsewhere.[21]

Figure 1b shows the setup of the present MC–DCFC system, which includes a carbon-filled full cell, a reference electrode (RE), and a gas supply tubing assembly for each electrode. The full cell (indicated with a dotted box) is schematically depicted in Figure 1c for comparison with the flat-plate cathode. Note that a 3 mm diameter copper tube was inserted into and then spot-welded to the cathode tube [used as a counter electrode (CE)] so that the Cu tube itself could be used as the electrical connection of the cathode and as the gas supply tube as well. The outer anode of the full cell was used as a working electrode (WE) to create electrons after being spot-welded to a flat-plate silver current collector. The RE, which was composed of a silver sheet and spot-welded to a silver wire, was sheathed in a 12 mm diameter alumina tube. Note that the RE is positioned 20 mm away from the full cell, which is sufficiently far away from the cell (i.e., the recommended greater than three electrolyte thicknesses) to eliminate any influence of the gradient in electrical potential near the electrodes.[27]

After mixing lithium carbonate (Li_2CO_3) and potassium carbonate (K_2CO_3) at a mole ratio of 62:38, 350 g of the mixture was heated to melt at 700 °C in the large alumina container, as shown in Figure 1b. A portion (50 mL min^{-1}) of carbon dioxide (CO_2) gas was supplied equally to the CE and the RE to flush out any residual gases before the experiment, while preheating the system. When the system temperature reached 700 °C, a gas mixture of CO_2 and O_2 (mole ratio 2:1) was supplied to the CE and the RE. Because the full cell (including the cathode) was fully submerged in the liquid electrolyte (MC), the gas mixture provided through the inner Cu tube was bubbled in the MC inside the cathode tube (as depicted in the left figure of Figure 1c) with the aim of increasing the physical contact between gas bubbles and the inner wall of the cathode. In contrast, a flat-plate silver cathode identical to the silver plate in the RE was also positioned within the MC so that the gas mixture blown into the MC should be diffused into the cathode through the MC pool to produce carbonate ions (refer to the right figure in Figure 1c).

To characterize our MC−DCFC system, we measured the difference in electrical potential between the WE and RE, the anode potential versus RE (V_a), and the cathode potential (V_C) between CE and RE by running an SP-150 potentiostat/galvanostat analyzer (NeoScience, Korea) at a scan rate of 1 mV s^{-1}. Similarly, the difference in cell potential (V) between the WE and CE was measured as a function of the electrical current between the WE and CE. The electrical current density (I) was obtained by dividing the measured cell current by the apparent contact area (A) between the cathode and anode (ca. 0.61 cm^2). As such, the power density (P) of the cell was calculated simply by multiplying the values of I and V. Moreover, electrochemical impedance spectroscopy (EIS) was performed on the full cell setup using the SP-150 analyzer in the frequency range of 0.06−80 kHz. Figure S2 in the Supporting Information describes the transient behaviors of temperature increase and open-circuit voltages (OCVs) during the preparation process prior to the I−V measurement. After the oxidant gas mixture was introduced to the CE and RE, the cell potential began to increase rapidly and then levelled off around the OCV in 90 min regardless of the cases. Then, the system was maintained at the OCV condition for 40 min before starting I−V measurement. After the I−V measurements, a durability test was conducted for the cells by monitoring the cell potential with time while maintaining the current density constant. We also monitored the composition of gas evolving from the anode under the MC during the durability test by connecting the exit of the carrier gas (see Figure 1b) to a gas chromatograph (Master GC, Dani Instruments).

3. RESULTS AND DISCUSSION

3.1. Comparative Analysis of the Case 1 Cell Performance for Component-Resolved Diagnosis.

The present tubular cell for case 1 was characterized by comparison with our previous three-electrode system,[21−23] in terms of the resistance of the anode, cathode, and cell, as well as the associated MPD.

When it comes to the I−V−P profiles in Figure 2a, case 1 shows a much more gradual slope of the profile of the cell potential (V_{Cell}) relative to the current density (I) than in the previous cell with no bubbling. This resulted in a 3-fold increase of cell MPD (as denoted by the solid triangles ▲ vs

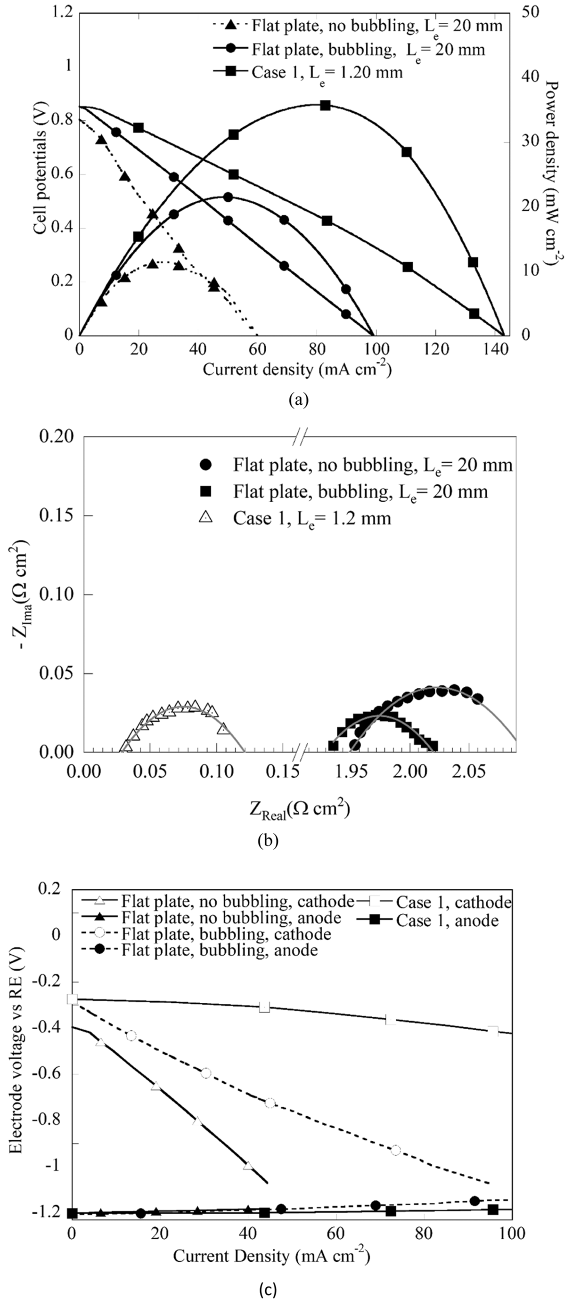

Figure 2. Electrochemical characteristics of the present full cell of case 1 in comparison with that of the previous half-cell with a flat-plate cathode in terms of (a) I−V−P profiles, (b) EIS profiles, and (c) electrode potentials at the anode and cathode vs I.

circles ●). Then, we carried out an additional case study on the previous system to clarify the role of oxidant bubbling, in which the oxidant gas supply tube was repositioned under the MC surface to bubble the gas in the vicinity of the submerged flat-plate cathode. As a result, bubbling the oxidant gas was determined to double the MPD (from 11.3 to 22.8 mW cm^{-2}), as denoted by the solid squares ■ versus circles ● in Figure 2a. It is noted that the I−V profiles are both seemingly linear. Because the slope in the straight section of the I−V curve represents the Ohmic resistance of the cell,[28−30] the observed increase of MPD for case 1 is likely attributable to a decrease in cell resistance, presumably resulting from the shortened anode-to-cathode distance between the electrodes (L_e: from 20.0 to 1.2 mm) and from bubbling of the oxidant gas as well.

To clarify this causal relationship, EIS measurements were performed under the OCV condition, and the results of the three cases are compared in Figure 2b. It should be noted that the left x intercept of the EIS semicircle for case 1, representing the electrolyte or solution resistance (R_{elec}), is substantially shifted to the left from the values of the flat-plate cathode with or without bubbling (from 1.93 to 1.95 to 0.03 Ω cm^2 for case 1). Also, the change in semicircle diameters indicates that the charge transfer resistance (R_{CT})[31−33] is slightly decreased from 0.14 to 0.08 Ω cm^2 upon bubbling.

To investigate further the behavior of the resistance with increasing I, we measured the electrical potential of the anode and cathode as a function of I using an RE, as shown in Figure 2c. Interestingly, the anode potential curves for the two cases are almost identical, manifesting the fact that the anode is unchanged. However, there is a large difference in the V_C profile. In contrast to the flat-plate cathode, the present cylindrical cathode in case 1 sustains a high level of V_C to achieve a higher current density, such that the cell potential (V_{Cell}) corresponding to the potential difference ($V_C - V_a$) can only slightly decrease with the current density until I ≤ 100mA cm^{-2}.

Here, the apparent resistance of each electrode was calculated directly from the slope of each potential curve. As a result, the cathode resistance (R_{Cat}) decreases from 14.1 Ω cm^2 for the previous cell without bubbling to 7.8 Ω cm^2 in the previous cell with bubbling and to 4.7 Ω cm^2 for case 1, while the anode resistance (R_{an}) is almost invariant (~0.4 Ω cm^2) in the three cases. Likewise, the cell resistance (R_{Cell}) decreases from 17.2 to 6.7 Ω cm^2 for case 1, as shown in Figure 2a. Combining these comparative analysis results, one may conclude that the bubbly flow of gas seems to enhance the cathode performance through the terms R_{CT} and R_{Cat}, probably by increasing contact with the cathode via the convective transport of gas.[34−36] Another thing to note is that this reduction of R_{Cat} is approximately two-thirds of that observed in case 1, suggesting that gas bubbling plays a considerable role in the cell operation. Also, in comparison with the previous cell, the present tubular cell for case 1 is obviously effective in further decreasing the resistance of the cathode and of the cell. However, the cell resistance is still as high as 6.7 Ω cm^2 due to being largely determined by the cathode. According to Jiang et al.,[10] a remarkable improvement in MPD was found upon reducing the cell resistance to <1 Ω cm^2, which suggests that the cathode of case 1 should be improved further to lower the cell resistance.

3.2. Transport of Carbonate Ions as a Rate-Limiting Step.

Despite the clear progress in cell performance, the power output of the full cell of case 1 was not satisfactory. To better understand the rate-limiting step, we considered the mass balance of carbonate ions inside the cathode tube from generation to transport toward the anode as

$$\frac{\partial C_R^*}{\partial t} \forall = \dot{g} - \dot{T} \tag{3}$$

where $\frac{\partial C_R^*}{\partial t}$ is the rate of change in the mole concentration (C_R^*) of carbonate ions inside the cathode tube with a volume ∀, $\dot{g}$ is the generation rate, and $\dot{T}$ is the transport rate of ions through the holes in units of moles per second. Based on the Faraday law, $\dot{g}$ is calculated directly from the measured current density I as $\dot{g} = IA/nF$, where F is the Faraday constant and n is the number of electrons in the cathode reaction in eq 2.

Recalling the low value of R_{CT} in the preceding section, the cathode reaction is simplified to consist of three successive sub-step reactions: diffusive transfer of the oxidant (i.e., O_2 + $2CO_2$ in eq 2) into the cathode, surface electrochemical conversion of the oxidant to reductant (i.e., carbonate ions), and diffusive transfer of the reductant into the MC from the cathode surface. At a certain current, each of the sub-step reactions would take place at a single (identical) rate to yield a stable (steady-state) current as

$$\dot{g} = \frac{IA}{nF} = m_R A(C_{R,S} - C_R^*) = m_O A(C_{O,S} - C_O^*) \tag{4}$$

Here, m_R and m_O represent the mass transfer coefficients of the reductant and oxidant, respectively (denoted by the subscripts R and O, respectively), $C_{R,S}$ and $C_{O,S}$ are the concentrations of the species at the surface, respectively, and C_O^* is the bulk concentration of the oxidant inside the cathode tube. The terms C_R^* and C_O^* are assumed to be spatially uniform inside the cathode due to vigorous mixing of the MC by bubbly flow.

The transport of carbonate ions is normally driven by the electrolyte potential gradient across the matrix. The local electrolyte potential φ_l can be produced by the existence of charge carriers (i.e., carbonate ions in this case), according to the Gauss law. In the Appendix, we described how to derive mathematical expressions on the spatial distribution of φ_l, particularly in the matrix. According to eq A3, the difference in the potential that drives the ions from the cathode hole to the anode surface is in linear proportion to C_R^* in the cathode tube. Hence, the ionic transport rate $\dot{T}$ through the holes can be expressed in connection with the electrical mobility (u_{ion}) and field strength ($-\mathrm{d}\varphi_l/\mathrm{d}x$) of ions as

$$\dot{T} = \frac{0 - \varphi_l(L_e)}{L_e} u_{\text{ion}} C_R^* n_h A_h \tag{5}$$

where n_h represents the number of holes, A_h is the opening area of a single hole, and the electrolyte potential at the anode surface $\varphi_l(0)$ is assumed to be zero in consideration of the fast anodic reaction.

Because $\dot{g} = \dot{T}$ at a steady state, the Faradaic current density I can be expressed using the systematic parameters by substituting eq A3 into eq 5 and equating eqs 4 and 5.

$$\frac{IA}{nF} = \frac{nF}{2\varepsilon_0\varepsilon_r}\left[\left(\frac{d}{4} + \frac{L_e}{3}\right)\right] C_R^* \cdot u_{\text{ion}} C_R^* n_h A_h \tag{6}$$

Note that the left-most term on the right side of eq 6 represents the potential gradient ($-\varphi_l(L_e)/L_e$), which is in linear proportion to C_R^*, and thus, $I \propto C_R^{*2} \cdot n_h$. Here, it should be noted that upon increasing I with a fixed n_h, the ion concentration C_R^* increases in proportion to $I^{1/2}$, which might create mass transfer overpotential and cause a rapid drop of V_C and V_{Cell}. Inversely, the larger n_h gives rise to lowering of the growth of C_R^* with increasing I, suggesting that the number of holes n_h is a key factor determining the current density and system performance.

This expectation became the motivation to increase the n_h further up to 84, as stated in Section 2, without altering the other parameters. Recalling that cases 2−4 correspond to n_h = 12, 24, and 84, respectively, we repeated the measurement of the $I-V-P$ profiles for the three cases and compare them in Figure 3. As a result, the MPD of the cell is obviously increased from 35 mW cm^{-2} for case 1 to 80, 130, and 205 mW cm^{-2} for cases 2−4, respectively, in response to a gradual decrease of the slope of the $I-V$ profile. From this slope, the cell resistance was correspondingly calculated to be 2.4, 1.26, and 1.09 Ω cm^2, respectively. At the same time, MCD was considerably increased, for example, reaching 1040 mA cm^{-2} for case 4. Because the only difference lies in the cathode, specifically in its ionic transport capacity, the increase of cell performance indicates that the cell resistance R_{Cell} is dominated by the cathode resistance R_{Cat}, which could be progressively improved by increasing n_h.

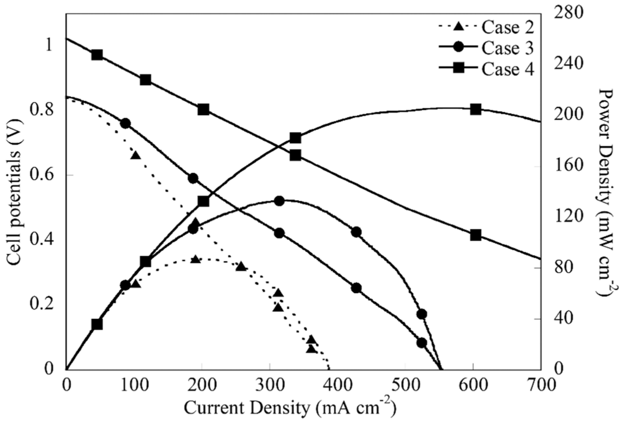

Figure 3. Comparison of $I-V-P$ characteristics of the present full cell in cases 2−4.

To confirm this speculation, we measured the cathode potentials versus RE (V_C) against the current density for the three cases. In Figure 4, the profiles of V_C look similar to the corresponding profiles of V_{Cell} in Figure 3. From the slope of each profile of V_C, we calculated the cathode resistance to confirm that the R_{Cat} decreases from 1.9 Ω cm^2 for case 2 to 0.75 and 0.6 Ω cm^2 for cases 3 and 4, respectively. Note that the values of R_{Cat} in cases 2−4 are 78.5, 63.5, and 55.0% of the R_{Cell}, respectively, such that the present cathode becomes the major factor determining the cell performance. More specifically, the R_{Cat} was halved by doubling the n_h in cases 2 and 3. This implies that the cathode of case 2 does not have enough capacity to transmit as many ions as required for the high current. This results in rapid decreases of the cathode and cell potentials, as shown in Figures 3 and 4. In cases 3−4, however, the 4-fold increase of n_h does not display such a dramatic decrease of R_{Cat} observed in cases 2−3, meaning that the ionic transport capacity $\dot{T}$ in case 3 is apparently large enough to handle a large number of ions, such that the intrinsic ion generation rate $\dot{g}$ of the cathode might begin to limit the cathode reaction rate in terms of resistance.

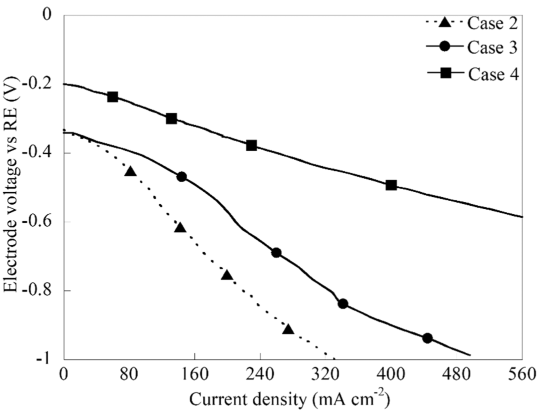

Figure 4. Comparison of cathode potential-to-current density profiles in cases 2−4.

What follows is an equation-based discussion on the coupling of the n_h and the cell resistance R_{Cell} through the C_R^*. On the cathode surface, the conversion reaction actually occurs by competition between the forward reaction in eq 2 and its backward (reverse) reaction.[37] Thus, the net reaction rate is expressed by

$$\frac{I}{nF} = k_f C_{O,S} - k_b C_{R,S} = k_0[C_{O,S}\, e^{-\alpha nF(V_c - V^0)} - C_{R,S}\, e^{(1-\alpha)nF(V_c - V^0)}] \qquad (7)$$

where k_f and k_b are the reaction rate constants for the forward and backward reactions, respectively, k_0 is the standard reaction rate constant, and V^0 is the formal potential. Accounting for vigorous mixing in the cathode, the two surface concentrations $C_{O,S}$ and $C_{R,S}$ can be correspondingly approximated to C_O^* and C_R^* (see eq 4), in connection with eq 6 (representing $I \propto C_R^{*2} \cdot n_h$); therefore, eq 7 provides a functional relationship between n_h and the cathode potential V_c. In case 1 (n_h = 1), the C_R^* grows the fastest (with increasing I according to eq 6) among the four cases. However, C_R^* is subjected to the minimal growth in case 4. In addition, both k_f and k_b are a sole function of V_c as $k_f = k_0 e^{-\alpha nF(V_c - V^0)}$ and $k_b = k_0 e^{(1-\alpha)nF(V_c - V^0)}$. This implies that k_f and k_b are both invariant between the cases when V_C is fixed. As such, it is evident that increasing n_h from cases 1 to 4 gives rise to an increase in the total current at a constant V_c by promoting the forward reaction in terms of $k_f C_O^*$ and impeding the backward reaction in terms of $k_b C_R^*$. Conversely, the potential V_C at a fixed current will decrease more rapidly in case 1 than in other cases to compensate the loss of net current resulting from decrease of C_O^* and increase of C_R^*. This behavior of V_C in case 1 would also appear to increase k_f and decrease k_b to sustain I [refer to the exponents in eq 7 ($-\alpha$ vs $1-\alpha$)].

To support the points proposed in the preceding discussion, we paid attention to the functional relationship in eq 6: $I \propto C_R^{*2} \cdot n_h$. From Figures 2a and 3, we extracted the values of current density ($I_{1/2}$) at $V_{Cell} = 1/2 V_{OC}$ for the four cases and calculated the relative concentration of ions, that is, $C^*_{R,nh}/C^*_{R,nh=1}$. In Figure 5, we plotted the relative concentration against n_h for comparison with the behavior of R_{Cat}. As a result, the relative concentration is well-correlated with the cathode

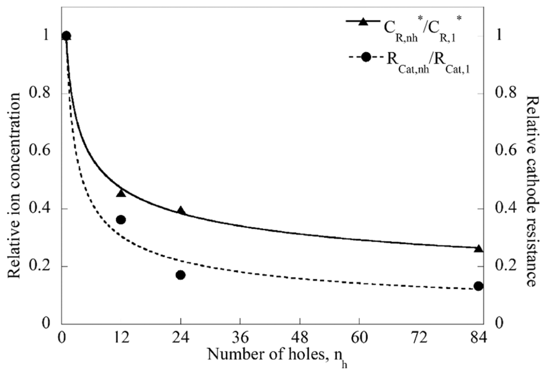

Figure 5. Variations of the relative concentration of carbonate ions in the cathode ($C^*_{R,nh}/C^*_{R,1}$) and the relative cathode resistance ($R_{Cat,nh}/R_{Cat,1}$) with respect to the number of holes (n_h).

resistance and shows a similar trend of decrease with the power of n_h: $\frac{C^*_{R,nh}}{C^*_{R,nh=1}} \propto n_h^{-0.3}$ and $\frac{R_{Cat,\,nh}}{R_{Cat,\,nh=1}} \propto n_h^{-0.48}$. It seems obvious that securing sufficient ion transport passage is essential for suppressing the mass transfer resistance of the cathode through the lower accumulation of ions in the cathode.

Next, we repeated the EIS measurements for cases 2−4 to measure R_{CT} and R_{elec}, which were then incorporated into the preceding data set of the elements and system that involves R_{an}, R_{Cat}, R_{Cell}, and MPD. After this, all of the aforementioned data were plotted against n_h in Figure 6 in an attempt to summarize the responses of the elements and system. Note that the condition in which the cathode resistance largely dominates the cell resistance shows a sharp drop with n_h between cases 1 and 2. Moreover, after reaching 79% above the anode resistance in case 3, the cathode resistance shows a slight decrease in case 4. In the latter two cases, because the cathode resistance is now less than twice as large as the anode resistance, the term R_{an} begins to play a role in determining the cell resistance and MPD. The figure also shows that the resistances R_{an} and R_{elec} are almost invariant, as expected from the fact that the anode and anode-to-cathode distance have not been changed. Overall, employing a metallic tubular cathode with a limited number of holes provides better experimental evidence for elucidating the role of the ion transport cross-section area in cathode resistance, as compared to the conventional porous cathodes used in DCFC systems.

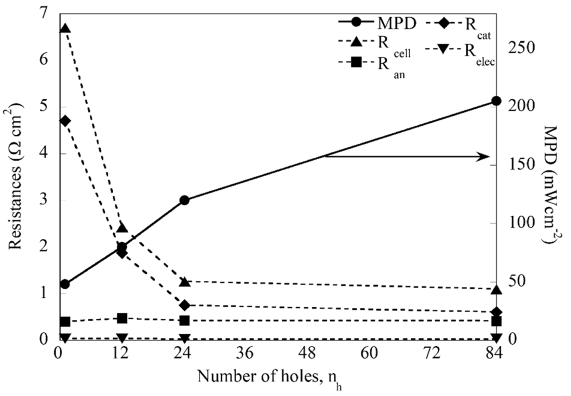

Figure 6. Effects of n_h on the resistances of the elements and the system as well as the MPD.

3.3. Long-Term Stability of the DCFC.

Long-term stability of DCFCs is one of the most critical concerns when developing a new type of DCFC system. For this stability test, we monitored the cell potential with increasing time at a constant current density of 50 mA cm^{-2} for cases 1 and 4. Figure 7 shows that the cell potential in case 1 decreases gradually from 0.6 to 0.3 V for the initial 50 min and then rapidly falls down to 0 V at 100 min. We believe that this behavior is closely related with the gradual accumulation of reductant species (carbonate ions) in the cathode, which leads to a rapid drop of cell potential far before the complete consumption of carbon fuels (see Section 3.2). In contrast, the potential in case 4 is maintained at around 0.9 V for 160 min and then gradually declines to 0.78 V for the next 150 min, followed by a cliff descent to 0 V at 314 min. Notably, the initial values of the potential in cases 1 and 4 (0.6 and 0.9 V, respectively) appear to be consistent with the potential values at I = 50 mA cm^{-2} in Figures 2a and 3. However, the cliff descent of cell potential in case 4 seems unnatural. Taking a close look at the raw data file for case 4, we realized that the sudden potential decrease from 0.77 to 0.58 V activated a safety protocol of the SP-150 analyzer to stop recording data. It is still unclear whether the sudden decrease of cell potential is real or a sort of artifact in the course of the emergency protocol (because the recorded time was unchanged during the last potential change). Excluding this, more importantly, the cell potential in case 4 was maintained above 0.77 V much longer than in case 1. As such, the unexpected accumulation of carbonate ions in cathode may be detrimental to MPD and stable operation of the DCFCs.

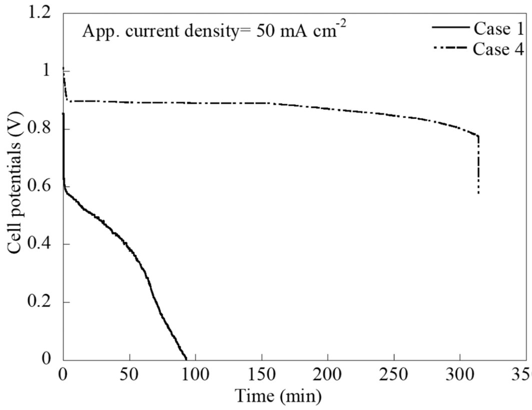

Figure 7. Long-term stability test results for the two cells of cases 1 and 4 at a fixed current density.

Lastly, it is interesting to verify whether or not any gaseous fuels were involved in the performance improvement in cases 1 to 4 including the enhanced durability, as shown in Figure 7. Since the oxidant gas mixture supplied to the RE and CE flows only through the alumina tube, the carbon fuels inside the anode become the only source of gaseous fuels such as CH_4, H_2, and CO[23] filling in the DCFC chamber (see Figure 1b). Furthermore, our carbon fuel is pure CNF with negligible volatile species, suggesting that the Boudouard reaction of CNF with CO_2 is the only possible pathway to produce CO inside the anode. Thus, we analyzed the composition of exhaust gas from the chamber using a gas chromatograph (see Section 2) with a focus on CO, in the beginning, middle, and near end of the durability test for case 4. As a result, there was

https://doi.org/10.1021/acsomega.2c03003
ACS Omega 2022, 7, 31003−31012

no sign of CO, but only CO_2 was found as a major species carried by Ar gas. The CO_2 concentration was almost invariant for ∼2.3% with time. The absence of CO in our DCFC chamber, however, does not necessarily indicate no contribution of CO to the MPD because the CO may be (electrochemically) oxidized to CO_2 before exiting the porous anode due to its higher reactivity than that of solid carbon.[10]

For the Boudouard reaction, Jalalabadi et al.[38] conducted a thermogravimetric analysis (TGA) for various raw coals and chars by flowing CO_2 gas and found that a char sample fabricated from a bituminous coal exhibits no mass decrease with the temperature increasing to up to 700 °C, meaning that the bituminous char is kinetically inert to gaseous CO_2 at the temperature. It is noteworthy that the bituminous char among the samples is the closest in nature to our CNF because it has the least amount of alkaline (catalytic) species in ash with no volatiles. Therefore, we conjecture that our CNF remain solid at 700 °C, not being converted to CO even at a partial pressure of CO_2 of 1 atm. In addition, the present anode was fully submerged in MC liquid, which is an unfavorable condition for the carbon conversion to CO as compared with the circumstance in TGA. Because of the buoyancy and low solubility of CO_2 gas in MC at 700 °C (see Table 1 of Claes et al.[39]), the CO_2 gas produced by the anodic reaction would be sent to the DCFC chamber rather than participate in the carbon conversion. Last, since the durability tests were performed using the same anode at a constant current density, there should be no difference in production rates of CO_2 and/or CO (if any) in the anode between the cases, contrary to the results in Figure 7. To sum up, all the foregoing discussion strongly indicates that the CNF are mainly (electrochemically) oxidized to CO_2 in the solid phase and the improved performance of case 4 does not relate to gaseous CO.

4. CONCLUSIONS

In this study, we developed a new tubular cell assembly comprising a carbon-filled porous anode, a thin matrix, and a tubular cathode with a certain number of holes for carbonate ion transport. In comparison with our previous half-cell consisting of an equivalent anode positioned 20 mm from a flat-plate cathode, the present full cell was initially anticipated to show excellent power generation by shortening the anode−cathode distance as well as bubbling the MC liquid. However, the first cell with a single hole was not quite as successful as expected, even though R_{CT} and R_{elec} were both reduced as expected. A resistance analysis by component revealed that the cathode exhibited a limitation in the mass transfer of carbonate ions toward the anode. By developing a distinctive current-potential model incorporating the ionic transport effect, we were enabled to propose that securing sufficient ion transport is the key to solving the problem, and finally, we were able to prove it. Specifically, simply increasing the number of holes was effective for lowering the cathode resistance to the vicinity of the anode resistance (∼0.4 Ω cm^2). This led to a significant increase of the MPD to 205 mW cm^{-2}. Unlike with conventional porous cathodes, the present cathode enabled the experimental determination of the significance of mass transport resistance in a DCFC by confining the ion transport to the predetermined holes. Despite the obvious technological progress described above, there is no objection that the DCFC technology is still far from its commercialization. Lastly, we would like to remind the state-of-the-art achievements in PEMFC as a goal we aim for: MPD > 978 mW cm^{-2} for 10,000 cycles[24] and minimal loss of durability over rapid freezing/melting cycles for a five cell stack of PEMFCs.[40]

APPENDIX

Electrolyte Potential at the Cathode−Matrix Interface

Figure A1 illustrates the spatial distribution of the electrolyte potential φ_l in the present cell. Inside a cathode tube with diameter d, carbonate ions generated from the cathode surface would be well-mixed by the bubbly flow in the MC so as to approximate a spatially uniform concentration of C_R^* at a fixed current. The negative ions existing in the MC can build up an electrolyte potential according to $\nabla^2\varphi_l = -\rho_v/\varepsilon_0\varepsilon_r$, where ε_0 is the vacuum permittivity, ε_r is the dielectric constant of the MC, and ρ_v is the volumetric charge density of the negative ions (relating to their local concentration C_R as $\rho_v = z_R F C_R$). Note that the charge number (z_R) of CO_3^{2-} is −2. Combining the two equations yields a governing equation to determine the φ_l as $\nabla^2\varphi_l = -\frac{z_R F}{\varepsilon_0\varepsilon_r}C_R$. Under the one-dimensional approximation, the Poisson equation for inside of the cathode was simplified to

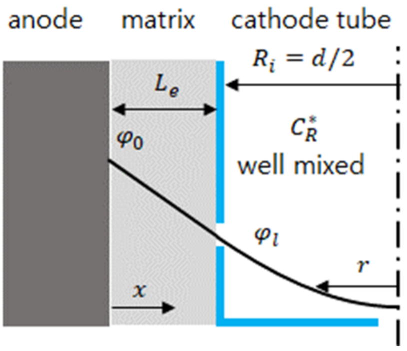

Figure A1. Schematic diagram of electrolyte potential distributions in the present cell with the definition of the spatial coordinates.

$$\frac{1}{r}\frac{d}{\mathrm{d}r}\left(r\frac{\mathrm{d}\varphi_l}{\mathrm{d}r}\right) = -\frac{z_R F}{\varepsilon_0\varepsilon_r}C_R^* \tag{A1}$$

Because the right-side term is a constant at a fixed current, integrating eq A1 over $0 \le r \le R_i$ yields the following two solutions.

$$\frac{\mathrm{d}\varphi_l}{\mathrm{d}r} = -\frac{z_R F}{2\varepsilon_0\varepsilon_r}C_R^*\mathrm{r};\ \ \varphi_l(r) = -\frac{z_R F}{4\varepsilon_0\varepsilon_r}C_R^* r^2 + \mathrm{const} \tag{A2}$$

Next, the Poisson equation was likewise solved for the matrix region in the Cartesian coordinate system for simplicity. The governing equation is $\frac{\mathrm{d}^2\varphi_l}{\mathrm{d}x^2} = -\frac{z_R F}{\varepsilon_0\varepsilon_r}C_R(x)$, where the source term is not a constant (unlike in eq A1). Here, $C_R(x)$ is approximated to vary linearly with x as $C_R(x) = \frac{x}{L_e}C_R^*$ due to the thinness of the matrix, meaning that the ion concentration at the anode surface is assumed to be zero. That is, $C_R(0) = 0$, which is appropriate given the fast anode reaction with very low R_{an} (see Section 3.2). The governing equation is integrated twice over x with two boundary conditions: $\varphi_l(0) = \varphi_0$ and $\left.\frac{\mathrm{d}\varphi_l}{\mathrm{d}x}\right|_{x=L_e} = -\left.\frac{d\varphi_l}{\mathrm{d}r}\right|_{r=R_i}$, yielding

$$\varphi_1(x) = -\frac{z_R F}{\varepsilon_0 \varepsilon_r}\left[\frac{x^3}{6L_e} - \left(\frac{d}{4} + \frac{L_e}{2}\right)x\right]C_R^* + \varphi_0 \tag{A3}$$

Here, the term in the bracket is negative across the matrix and $z_R = -2$, so the electrolyte potential difference $(\varphi_1 - \varphi_0)$ keeps decreasing with x, as illustrated in Figure A1.

■ ASSOCIATED CONTENT

Supporting Information

The Supporting Information is available free of charge at https://pubs.acs.org/doi/10.1021/acsomega.2c03003.

> General preparation process of the carbon-loaded porous anode and its characteristics prior to I−V measurement and structural visualization of the carbon-loaded porous Ni anode in a cathode-supported DCFC (PDF)

■ AUTHOR INFORMATION

Corresponding Author

Donggeun Lee − *School of Mechanical Engineering, Pusan National University, Busan 46241, South Korea;* orcid.org/0000-0001-7256-1956; Email: donglee@pusan.ac.kr

Authors

Raihan Choudhury − *School of Mechanical Engineering, Pusan National University, Busan 46241, South Korea;* orcid.org/0000-0002-9626-0469

Ah-Hyun Kang − *School of Mechanical Engineering, Pusan National University, Busan 46241, South Korea*

Complete contact information is available at: https://pubs.acs.org/10.1021/acsomega.2c03003

Notes

The authors declare no competing financial interest.

■ ACKNOWLEDGMENTS

This work was supported by a Korea Institute of Energy Technology Evaluation and Planning (KETEP) grant funded by the Korea government (MOTIE) (20214000000140, Graduate School of Convergence for Clean Energy Integrated Power Generation) and also by a National Research Foundation of Korea (NRF) grant funded by the Korea government (MSIT) (NRF-2020R1A2C2011634).

■ REFERENCES

(1) Giddey, S.; Badwal, S. P. S.; Kulkarni, A.; Munnings, C. A Comprehensive Review of Direct Carbon Fuel Cell Technology. *Prog. Energy Combust. Sci.* **2012**, *38*, 360−399.

(2) Cao, D.; Sun, Y.; Wang, G. Direct Carbon Fuel Cell: Fundamentals and Recent Developments. *J. Power Sources* **2007**, *167*, 250−257.

(3) Elleuch, A.; Boussetta, A.; Halouani, K. Analytical Modeling of Electrochemical Mechanisms in CO2 and CO/CO2 Producing Direct Carbon Fuel Cell. *J. Electroanal. Chem.* **2012**, *668*, 99−106.

(4) Vutetakis, D. G.; Skidmore, D. R.; Byker, H. J. Electrochemical Oxidation of Molten Carbonate-Coal Slurries. *J. Electrochem. Soc.* **1987**, *134*, 3027.

(5) Dudek, M.; Tomczyk, P.; Socha, R.; Hamaguchi, M. Use of ash-free "Hyper-coal" as a fuel for a direct carbon fuel cell with solid oxide electrolyte. *Int. J. Hydrogen Energy* **2014**, *39*, 12386−12394.

(6) Vu, D.-L.; Lee, C.-G. Oxidation of Ash-Free Coal from Sub-Bituminous and Bituminous Coals in a Direct Carbon Fuel Cell. *Korean J. Chem. Eng.* **2016**, *33*, 507−513.

(7) Kaklidis, N.; Garagounis, I.; Kyriakou, V.; Besikiotis, V.; Arenillas, A.; Menéndez, J. A.; Marnellos, G. E.; Konsolakis, M. Direct utilization of lignite coal in a Co-CeO 2 /YSZ/Ag solid oxide fuel cell. *Int. J. Hydrogen Energy* **2015**, *40*, 14353−14363.

(8) Li, X.; Zhu, Z. H.; Marco, R.; Dicks, A.; Bradley, J.; Liu, S.; Lu, G. Q. Factors That Determine the Performance of Carbon Fuels in the Direct Carbon Fuel Cell. *Ind. Eng. Chem. Res.* **2008**, *47*, 9670−9677.

(9) Li, X.; Zhu, Z.; De Marco, R.; Bradley, J.; Dicks, A. Carbon Nanofibers Synthesized by Catalytic Decomposition of Methane and Their Electrochemical Performance in a Direct Carbon Fuel Cell. *Energy* **2009**, *23*, 3721−3731.

(10) Jiang, C.; Ma, J.; Corre, G.; Jain, S. L.; Irvine, J. T. S. Challenges in Developing Direct Carbon Fuel Cells. *Chem. Soc. Rev.* **2017**, *46*, 2889−2912.

(11) Gür, T. M. Critical Review of Carbon Conversion in Carbon Fuel Cells. *Chem. Rev.* **2013**, *113*, 6179−6206.

(12) Wang, F.; Deng, S.; Zhang, H.; Wang, J.; Zhao, J.; Miao, H.; Yuan, J.; Yan, J. A Comprehensive Review on High-Temperature Fuel Cells with Carbon Capture. *Appl. Energy* **2020**, *275*, 115342.

(13) Bie, K.; Fu, P.; Liu, Y.; Muhammad, A. Comparative Study on the Performance of Different Carbon Fuels in a Molten Carbonate Direct Carbon Fuel Cell with a Novel Anode Structure. *J. Power Sources* **2020**, *460*, 228101.

(14) Bartoli, M.; Giorcelli, M.; Jagdale, P.; Rovere, M.; Tagliaferro, A. A Review of Non-Soil Biochar Applications. *Materials* **2020**, *13*, 261.

(15) Kulkarni, A.; Giddey, S.; Badwal, S. P. S. Electrochemical Performance of Ceria-Gadolinia Electrolyte Based Direct Carbon Fuel Cells. *Solid State Ionics* **2011**, *194*, 46−52.

(16) Liu, R.; Zhao, C.; Li, J.; Zeng, F.; Wang, S.; Wen, T.; Wen, Z. A Novel Direct Carbon Fuel Cell by Approach of Tubular Solid Oxide Fuel Cells. *J. Power Sources* **2010**, *195*, 480−482.

(17) Hao, W.; He, X.; Mi, Y. Achieving High Performance in Intermediate Temperature Direct Carbon Fuel Cells with Renewable Carbon as a Fuel Source. *Appl. Energy* **2014**, *135*, 174−181.

(18) Jiang, C.; Ma, J.; Bonaccorso, A. D.; Irvine, J. T. S. Demonstration of High Power, Direct Conversion of Waste-Derived Carbon in a Hybrid Direct Carbon Fuel Cell. *Energy Environ. Sci.* **2012**, *5*, 6973.

(19) Jayakumar, A.; Küngas, R.; Roy, S.; Javadekar, A.; Buttrey, D. J.; Vohs, J. M.; Gorte, R. J. A Direct Carbon Fuel Cell with a Molten Antimony Anode. *Energy Environ. Sci.* **2011**, *4*, 4133.

(20) Ju, H.; Uhm, S.; Kim, J. W.; Song, R. H.; Choi, H.; Lee, S. H.; Lee, J. Enhanced Anode Interface for Electrochemical Oxidation of Solid Fuel in Direct Carbon Fuel Cells: The Role of Liquid Sn in Mixed State. *J. Power Sources* **2012**, *198*, 36−41.

(21) Li, C.; Yi, H.; Lee, D. On-Demand Supply of Slurry Fuels to a Porous Anode of a Direct Carbon Fuel Cell: Attempts to Increase Fuel-Anode Contact and Realize Long-Term Operation. *J. Power Sources* **2016**, *309*, 99−107.

(22) Li, C.; Yi, H.; Jalalabadi, T.; Lee, D. Thermal Decomposition of Alkane Hydrocarbons inside a Porous Ni Anode for Fuel Supply of Direct Carbon Fuel Cell: Effects of Morphology and Crystallinity of Carbon. *J. Power Sources* **2015**, *294*, 284−291.

(23) Li, C.; Yi, H.; Eom, S.; Choi, G.; Choi, T. Y.; Lee, D. Intrinsic Solid-State Reaction Characteristics of Coals and Chars in a Direct Carbon Fuel Cell: With Focus on Significance Assessment of Fuel-Borne Factors. *Energy Fuels* **2020**, *34*, 4129−4138.

(24) Wang, H.; Lin, R.; Cai, X.; Liu, S.; Zhong, D.; Hao, Z. Transition Metal Dissolution Control in Pt-Alloy Catalyst Layers for Low Pt-Loaded PEMFCs for Improving Mass Transfer. *Int. J. Heat Mass Transfer* **2021**, *178*, 121615.

(25) Lan, R.; Tao, S. A Simple High-Performance Matrix-Free Biomass Molten Carbonate Fuel Cell without CO 2 Recirculation. *Sci. Adv.* **2016**, *2*, 1600772.

(26) Cao, T.; Huang, K.; Shi, Y.; Cai, N. Recent advances in high-temperature carbon-air fuel cells. *Energy Environ. Sci.* **2017**, *10*, 460–490.

(27) Adler, S.; Henderson, B. T.; Wilson, M. A.; Taylor, D. M.; Richards, R. E. Reference Electrode Placement and Seals in Electrochemical Oxygen Generators. *Solid State Ionics* **2000**, *134*, 35–42.

(28) Eom, S.; Ahn, S.; Kang, K.; Choi, G. Modeling Electrochemical Resistance with Coal Surface Properties in a Direct Carbon Fuel Cell Based on Molten Carbonate. *J. Power Sources* **2017**, *372*, 54–63.

(29) Zhang, P.-Y.; Liu, Z.-L. Experimental Study of the Microbial Fuel Cell Internal Resistance. *J. Power Sources* **2010**, *195*, 8013–8018.

(30) Zhang, J.; Jiang, X.; Piao, G.; Yang, H.; Zhong, Z. Simulation of a Fluidized Bed Electrode Direct Carbon Fuel Cell. *Int. J. Hydrogen Energy* **2015**, *40*, 3321–3331.

(31) Kang, M. G.; Song, S. A.; Jang, S. C.; Oh, I. H.; Han, J.; Yoon, S. P.; Kim, S. H.; Oh, S. G. Fabrication of Electrolyte-Impregnated Cathode by Dry Casting Method for Molten Carbonate Fuel Cells. *Korean J. Chem. Eng.* **2012**, *29*, 876–885.

(32) Hu, L.; Rexed, I.; Lindbergh, G.; Lagergren, C. Electrochemical Performance of Reversible Molten Carbonate Fuel Cells. *Int. J. Hydrogen Energy* **2014**, *39*, 12323–12329.

(33) O'Hayre, R.; Cha, S.-W.; Colella, W.; Prinz, F. B. *Fuel Cell Fundamentals*; John Wiley & Sons, Inc: Hoboken, NJ, USA, 2016.

(34) Zhao, X.; Ren, H.; Luo, L. Gas Bubbles in Electrochemical Gas Evolution Reactions. *Langmuir* **2019**, *35*, 5392–5408.

(35) Birkin, P. R.; Watson, Y. E.; Leighton, T. G. Communication Efficient Mass Transfer from an Acoustically Oscillated Gas Bubble. *Chem. Commun.* **2001**, 2650.

(36) Bergman, T. L.; Incropera, F. P. *Fundamentals of Heat and Mass Transfer*; John Wiley & Sons, 2011; p 1048.

(37) Nagase, K.; Shimodaira, T.; Itoh, M.; Zheng, Y. Kinetics and Mechanisms of the Reverse Boudouard Reaction over Metal Carbonates in Connection with the Reactions of Solid Carbon with the Metal Carbonates. *Phys. Chem. Chem. Phys.* **1999**, *1*, 5659–5664.

(38) Jalalabadi, T.; Li, C.; Yi, H.; Lee, D. A TGA study of CO2 gasification reaction of various types of coal and biomass. *J. Mech. Sci. Technol.* **2016**, *30*, 3275–3281.

(39) Claes, P.; Thirion, B.; Glibert, J. Solubility of CO, in the Molten Na_2CO_3-K_2CO_3 (42 Mol %) in Eutectic Mixture at 800°C. *Electrochim. Acta* **1996**, *41*, 141–146.

(40) Zhong, D.; Lin, R.; Jiang, Z.; Zhu, Y.; Liu, D.; Cai, X.; Chen, L. Low Temperature Durability and Consistency Analysis of Proton Exchange Membrane Fuel Cell Stack Based on Comprehensive Characterizations. *Appl. Energy* **2020**, *264*, 114626.

https://doi.org/10.1021/acsomega.2c03003
ACS Omega 2022, 7, 31003–31012